nature portfolio

Peer Review File

Dual deconvolution in multiphoton structured illumination microscopy for deep-tissue super-resolution imaging

Corresponding Author: Professor Wonshik Choi

This file contains all reviewer reports in order by version, followed by all author rebuttals in order by version.

Version 0:

Reviewer comments:

Reviewer #1

(Remarks to the Author)
Comments to authors:

This article by Choi and Yoon presents a unique approach to achieve super-resolution imaging in multiphoton scanning microscopy in aberrating media. The authors use a modified version of a technique known as image scanning microscopy (ISM) that captures images of the emitted point spread function in a laser scanning microscope setup. They demonstrate their novel approach of leveraging the diversity of illumination intensity angles and phase shifts present in the imaged PSF that naturally emerge during point scanning to perform an alternate version of structured illumination. This enables dual-deconvolution computational adaptive optics for the excitation and emission light. Their calculated theoretical resolution is 140nm, which is very impressive for distorting media. In practice, they find closer to 175nm through a scattering phantom and 240nm without scattering media. The manuscript is thorough, and presents a compelling case for the novelty and impact of the proposed concept. However, some additional experiments are needed to conclusively demonstrate the technique and to compare with similar current best practices. One notable lack is in the comparison between the described approach and standard ISM. Further discussion of this would help to strengthen the manuscript. Although the manuscript requires revision, the approach is cutting edge and constitutes a significant advance in the use of computational and hardware approaches to create super-resolution images in living animals. It seems to be of sufficient impact for publication in Nat Commun and is likely to be of interest to the journal's readership.

Additional comments:

-Given that this paper presents an enhanced version of image scanning microscopy, a direct comparison in the theoretical and attainable resolution versus typical ISM pixel reassignment reconstructions that have been implemented in the past would be relevant to include in the text and figures.

-Lines 122-125— While the details of the dual-deconvolution in the methods seems to make sense to this reviewer, the description in the results is harder to follow. It is seems reasonable that the idea of tuning the phase of each spectrum to enhance the intensity of the synthesized spectrum will help with the excitation aberrations. Figure 1 does a decent job of alluding to this possibility. However, it is somewhat less clear in the text and figure 1 how the modification of the spectral map (as described in lines 137-138) is performed for the emission.

-Lines 160 and following, 403 and following, and Figure 2— The authors state that "the excitation and emission pupil maps were computationally prepared by the random superposition of Zernike modes numbering up to 30." How many random combinations were tested? What type/depth of tissue aberrations is this hoping to mimic? Were the random aberrations different between emission and excitation, and how realistic is this combination?

-Are signal loss, noise and tissue scattering (or even aberrations beyond Zernike mode 30) likely to play a role in the limitations of the approach? This is mentioned briefly in the discussion, but additional information could be helpful.

-Figure 3 and lines 208-219— The bead separation measurement is insightful, but what was the experimentally measured size of the sub-diffraction beads? How close does this come to the theoretical predictions?

-It would be interesting to see the calculated excitation and emission Zernike modes for some of the samples displayed. How stable are the optimized Zernike modes for a given set of aberrated images?

-Figure S3— Since the idea of isoplanatic patch is mentioned, it could support the concept to calculate the isoplanatic patch size for the image shown. This could be accomplished by applying the optimized Zernike modes to neighboring locations.

-line 312— A little bit more discussion about other approaches to speed imaging in ISM and alternate detectors (e.g. SPAD cameras) prior to the concluding paragraph could help to strengthen the case for future impact of the work.

(Remarks on code availability)

Reviewer #2

(Remarks to the Author)
This manuscript presents a solid advancement in multiphoton super-resolution imaging through the development of a computational adaptive optics (AO) framework based on virtual structured illumination microscopy (SIM). A central innovation is the dual deconvolution algorithm, which iteratively corrects excitation and emission aberrations using Wiener-like updates to solve for three unknowns (i.e., object, excitation OTF, and emission OTF), thus decomposing a complex optimization problem into well-conditioned, tractable subproblems. While the spectral synthesis concept underlying the two-photon SIM implementation is similar to the recently established k-space interpretation of image scanning microscopy in the single-photon regime, the proposed dual deconvolution process represents a novel and effective computational strategy. The use of virtual, rather than real, structured illumination enables the adaptive correction of aberrations, achieving 130 nm lateral resolution at a depth of 180 μm in thick mouse brain tissue. The manuscript is technically sound, with a clearly described algorithmic workflow, comprehensive experimental details, and results that support the applicability of the approach. Overall, this work makes a meaningful contribution to the field and offers a promising computational solution for deep-tissue super-resolution imaging.

A limitation of the manuscript is the restricted generalizability of the approach. Specifically, the computational adaptive optics framework applies only to virtual structured illumination, which inherently limits imaging speed. Accelerating acquisition would require multifocal scanning strategies, typically involving the capture of hundreds of images, representing a significant weakness compared to hardware AO systems. Additionally, the dual deconvolution algorithm depends on the unique separable structure of the excitation and emission OTFs (Hex and Hem), which is essential for making the problem tractable in this context. Whether this algorithm can be extended to other applications remains unclear and is not discussed in the manuscript.

Another limitation lies in the biological demonstrations, which are somewhat limited, featuring only a thin cell and a thick sample with only a few xy planes but lacking any 3D volumetric data. While the lateral resolution enhancement is evident, axial resolution and performance are not discussed. As the deconvolution is currently applied only in 2D, the authors may consider discussing potential extensions of the dual deconvolution algorithm to fully exploit super-resolution capabilities in three dimensions. In addition, Supplementary Figure 3, which presents zebrafish imaging, appears more compelling than Figure 5, as it shows a more pronounced improvement after computational AO correction and effectively demonstrates the method's ability to address challenging cases with spatially varying aberrations.

Minor comments:
1) The data processing speed is not discussed, including the spatially varying iterations for multiple regions.
2) Line 100, ki is not well defined
3) Line 104, alpha (numerical aperture?) is not defined.
4) Fig. 5(g), the dash lines 1-5 seem off from the spine neck.

(Remarks on code availability)

Reviewer #3

(Remarks to the Author)
Advantages

1. Interesting idea. The author proposed a dual deconvolution computational aberration correction (AO) algorithm that corrects for aberrations in both excitation and emission in multiphoton deep-tissue structured illumination microscopy (SIM).
2. No additional hardware required. The proposed method doesn't require complex wavefront shaping or sensing devices.
3. Good experimental results. The improvements in aberration correction and resolution are clearly demonstrated.
4. Code and data are available online, which will benefit the community.

Weakness

1. Computational AO methods generally suffer from low SNR, especially when applied to deep tissue imaging. All experimental results provided by the authors have very high SNR. The paper lacks analysis of how SNR affects the

reconstruction quality.
2. The reconstruction quality in SIM algorithms is highly dependent on the modulation depth or contrast of the illumination pattern, which tends to degrade after propagating through a scattering medium. How do the authors address this issue? And how significantly does this degradation affect the final reconstruction quality?
3. From a practical standpoint, also as an echo to earlier points, the proposed algorithm is a sophisticated but still blind deconvolution/non-convex optimization method. This kind of approach can be prone to getting trapped in local minima, especially when dealing with complex OTF shapes. The authors highlight that their method requires no prior knowledge of the PSF (as noted in lines 425–426 and 431), and that it uses only simple regularization (line 360, section "Dual deconvolution algorithm"). Given this, is there a risk that the algorithm may fail to recover the PSF in certain conditions? I would expect to see examples where the method struggles, such as particular types of excitation/emission PSFs or sample structures that may pose challenges.

(Remarks on code availability)

Version 1:

Reviewer comments:

Reviewer #1

(Remarks to the Author)
No further comments

(Remarks on code availability)

Reviewer #2

(Remarks to the Author)
The authors have adequately addressed my comments. I recommend its publication.

(Remarks on code availability)

Reviewer #3

(Remarks to the Author)
I appreciate the new results provided by the authors. The proposed method is well-demonstrated through comprehensive analysis and I expect it will be applicable to future SIM applications. All my concerns have been addressed and I suggest accept the manuscript.

(Remarks on code availability)

Reviewer #1

Reviewer's comment: *This article by Choi and Yoon presents a unique approach to achieve super-resolution imaging in multiphoton scanning microscopy in aberrating media. The authors use a modified version of a technique known as image scanning microscopy (ISM) that captures images of the emitted point spread function in a laser scanning microscope setup. They demonstrate their novel approach of leveraging the diversity of illumination intensity angles and phase shifts present in the imaged PSF that naturally emerge during point scanning to perform an alternate version of structured illumination. This enables dual-deconvolution computational adaptive optics for the excitation and emission light. Their calculated theoretical resolution is 140nm, which is very impressive for distorting media. In practice, they find closer to 175nm through a scattering phantom and 240nm without scattering media. The manuscript is thorough, and presents a compelling case for the novelty and impact of the proposed concept. However, some additional experiments are needed to conclusively demonstrate the technique and to compare with similar current best practices. One notable lack is in the comparison between the described approach and standard ISM. Further discussion of this would help to strengthen the manuscript. Although the manuscript requires revision, the approach is cutting edge and constitutes a significant advance in the use of computational and hardware approaches to create super-resolution images in living animals. It seems to be of sufficient impact for publication in Nat Commun and is likely to be of interest to the journal's readership.*

Response: We thank the reviewer for the thoughtful and constructive evaluation of our manuscript. We are grateful for the recognition of the novelty, rigor, and potential impact of our method, as well as the helpful suggestions for further clarification and validation, particularly the request for a direct comparison with conventional image scanning microscopy (ISM). We performed additional simulations and analyses and added a unified theoretical framework for image reconstruction from fluorescence response function in Supplementary Information (SI). Below, we provide detailed point-by-point responses and indicate how each comment has been addressed. Figures referenced in this response letter (Figs. R1-10) are included at the end of this document.

Reviewer's comment: *Given that this paper presents an enhanced version of image scanning microscopy, a direct comparison in the theoretical and attainable resolution versus typical ISM pixel reassignment reconstructions that have been implemented in the past would be relevant to include in the text and figures.*

Response: We appreciate the reviewer's insightful suggestion to include a direct theoretical and experimental comparison between the proposed method and standard ISM pixel reassignment. In response, we have added a comprehensive analysis in SI Section 2, where we present a unified theoretical framework that relates ISM pixel reassignment and SIM spectral synthesis within a common representational domain.

Essentially, the optical transfer functions of ISM and SIM can be expressed as

$$H_{\mathrm{ISM}}(k) = H_{\mathrm{em}}\left(\frac{k}{2}\right) H_{\mathrm{ex}}\left(\frac{k}{2}\right),\ H_{\mathrm{SIM}} = H_{\mathrm{em}} * H_{\mathrm{ex}},$$

where * denotes convolution. Therefore, both methods achieve comparable bandwidth extension in theory but differ in their modulation transfer function (MTF) weightings, affecting robustness to noise and aberration.

We supplemented the theory with simulations and experimental data, as shown in Figures R1–R3:

Figure R1 illustrates representative image-reconstruction operations of ISM and SIM in both real and spatial-frequency spaces, alongside wide-field (WF), laser-scanning (LS), and confocal (CON) modalities for reference.

Figure R2 provides a direct comparison of five imaging modes (LS, CON, ISM, SIM, AO-SIM) in their reconstructed images from the identical fluorescence-response datasets under three conditions: ideal simulation (no aberration), a resolution-target experiment (strong aberration), and a live-cell experiment

(mild aberration). Under ideal conditions, CON, ISM, and SIM achieve comparable resolution (Fig. R2a), whereas their performance diverges in aberrated and noisy environments (Figs. R2b–c). AO-SIM image demonstrates markedly improved image recovery in all cases.

Figure R3 presents the effective MTFs for ISM and SIM under representative aberrations. Although both cover the same bandwidth, their MTF weightings differ, leading to characteristic attenuation and distortion behaviors. Importantly, the dual-deconvolution algorithm restores the spectrum across the entire frequency range, maintaining both resolution and contrast.

These results demonstrate that while ISM and SIM offer comparable nominal resolution, our method of AO-SIM maintains superior performance in realistic, aberrated environments through explicit correction of both excitation and emission distortions.

Reviewer's comment: *Lines 122-125— While the details of the dual-deconvolution in the methods seems to make sense to this reviewer, the description in the results is harder to follow. It seems reasonable that the idea of tuning the phase of each spectrum to enhance the intensity of the synthesized spectrum will help with the excitation aberrations. Figure 1 does a decent job of alluding to this possibility. However, it is somewhat less clear in the text and figure 1 how the modification of the spectral map (as described in lines 137-138) is performed for the emission.*

Response: We thank the reviewer for pointing this out. We have revised the manuscript to provide the intuitive explanation for the emission OTF estimation. The key concept is optical reciprocity. First, we apply phase-tuning/synthesis to estimate the excitation OTF phase. We then apply the identical procedure to the transposed response matrix, $F^{\mathrm{T}}(\mathbf{k}_{\mathrm{i}}, \mathbf{k}_{\mathrm{d}})$ to estimate the emission OTF. Transposing the response matrix is physically equivalent to interchanging (swapping) illumination and detection sides. Therefore, optimizing the synthesized spectrum of F^{T} allows for the estimation of the emission OTF. We have added the following explanation to the main text:

"An intuitive explanation is to tune the overall phase of each spectrum in Fig. 1d to maximize the total intensity of the synthesized spectrum in Fig. 1e, which yields an estimate of H_{ex}. A similar operation is conducted on the reciprocal basis (interchanging $\mathbf{k}_{\mathrm{i}}$ and $\mathbf{k}_{\mathrm{d}}$) to estimate H_{em}. By optical reciprocity, swapping the illumination and detection ports yields the transpose of the response, $F^{\mathrm{T}}(\mathbf{k}_{\mathrm{i}}, \mathbf{k}_{\mathrm{d}})$, representing the same optics traversed in reverse: the overall phase that previously resided on the illumination side now appears on the detection side. Accordingly, we apply the same spectral synthesis and phase tuning to F^{T}, maximizing the total intensity of the synthesized (transposed) spectrum to obtain the estimate of H_{em}. Iterating these two paths drives the synthesized spectrum toward maximum total intensity (see Methods for detailed mathematical description)."

Reviewer's comment: *Lines 160 and following, 403 and following, and Figure 2— The authors state that "the excitation and emission pupil maps were computationally prepared by the random superposition of Zernike modes numbering up to 30." How many random combinations were tested? What type/depth of tissue aberrations is this hoping to mimic? Were the random aberrations different between emission and excitation, and how realistic is this combination?*

Response: We appreciate this important question. A detailed description of the pupil aberration modeling has been added to the SI. We tested the algorithm's performance over a broad range of random aberration combinations generated by random superpositions of Zernike modes.

The aberrations simulated in Fig. 2 and experimentally demonstrated in Figs. 4f–k are comparable in strength and complexity to those typically encountered in imaging through thinned-skull mouse preparations of approximately 30–100 μm thickness, as reported in *Nat. Commun.* **11,** 5721 (2020) and *Nat. Biotechnol.* **40,** 1663–1671 (2022). For the COS-7 cell and mouse brain tissue experiments shown in Fig. 5, the aberrations are relatively mild, consistent with the levels described in *PhotoniX* **4,** 38 (2023) and *Nat. Methods* **14,** 869 (2017). The zebrafish data (now relocated from the SI to the main text, Fig. 6) exhibit aberration magnitudes in agreement with prior *in vivo* optical imaging studies (*Nat. Commun.* **10,** 3152 (2019)).

In general, for one-photon fluorescence imaging, excitation and emission paths experience nearly identical aberrations because of their similar wavelengths. However, in two-photon imaging, these paths can differ substantially. The longer excitation wavelength experiences reduced phase retardation for the same optical-path difference, owing to the inverse wavelength ($1/\lambda$) dependence of phase. Therefore, explicit correction of both excitation and emission aberrations is essential to maximize image quality, as also emphasized in *PhotoniX* **4,** 38 (2023).

Importantly, our dual-deconvolution algorithm does not rely on prior knowledge of, or structural assumptions about, either PSF. It operates robustly even when excitation and emission aberrations are completely uncorrelated. To demonstrate this capability, the simulations presented in Fig. 2 intentionally employed strong, mutually independent aberrations for the excitation and emission pupils. This design choice highlights the algorithm's ability to recover high-fidelity images under realistic and highly aberrated conditions.

Reviewer's comment: *Are signal loss, noise and tissue scattering (or even aberrations beyond Zernike mode 30) likely to play a role in the limitations of the approach? This is mentioned briefly in the discussion, but additional information could be helpful.*

Response: Thank you for raising this important point. We have addressed this in SI Sections 4–6, where we systematically evaluate noise sensitivity, aberration strength, and aberration complexity.

(1) Analysis of SNR and resolution

We conducted a SNR analysis while maintaining aberration strength and complexity (Fig. R4). Independent excitation and emission pupil functions were numerically generated using Zernike modes up to N=30 (piston and tilt excluded), yielding 505 modes in total. From the corresponding OTFs, fluorescence response functions were simulated over a range of noise levels, and AO-2PSIM images were reconstructed via dual deconvolution. As the SNR of the 2PSIM images decreased, the recoverable high-frequency information in the effective OTFs diminished (as shown in the PTF images in Fig. R4), leading to reduced fidelity in both the recovered and corrected PSFs. The algorithm maintains reasonable performance down to SNR≈4 (measured from the 2PSIM images), consistent with the SNR≈4 estimated for the dataset in Fig. 4h (main text). Below this level, the fidelities of both the recovered target images and the PSFs degrade.

Fourier ring correlation (FRC) curves obtained from 2PSIM images at various SNR conditions show resolution degradation with increasing noise before aberration correction (Fig. R5a). In contrast, FRC curves from AO-2PSIM images mostly demonstrate higher cut-off frequencies (Fig. R5b). The direct visualization of these cut-off frequencies (Fig. R5c) shows the bandwidth recovery capability of the dual deconvolution method.

To further validate this, we performed 10 independent simulation runs at each SNR level and calculated SNR-enhancement factors and resolutions. The results show that our method improves SNR by up to 8-fold (Fig. R5d), and super-resolution (cut-off frequency $> 3\alpha k_{em}$, i.e., resolution $< \lambda_{em}/3\alpha$) is achievable at SNR≈4. These quantitative SNR-resolution correlations clarify the performance of dual deconvolution across diverse noise and aberration conditions.

(2) Analysis of aberration strength

To quantify dual-deconvolution performance as aberration strength increases, we conducted a simulation study under ideal noise-free conditions using Zernike modes up to N=30 (Fig. R6). The Zernike-coefficient magnitudes were systematically scaled to control aberration strength, and reconstruction quality was assessed by the Pearson correlation (PC) between the recovered and ground-truth PSFs. As aberration strength increases, PC values decrease, consistent with reduced high-frequency support in the reconstructed OTFs. At higher aberration levels, the loss of high-frequency content primarily limits the achievable resolution and renders fine structural details.

(3) Analysis of aberration complexity

We extended the analysis to aberration complexity by increasing the number of Zernike modes from N=30 to N=120 (Fig. R7). As complexity increased, the recovered OTFs exhibited increasingly complex phase structures, and PC between reconstructed and ground-truth images steadily declined, indicating a reduction in resolution and accuracy of retrieved OTFs and PSFs.

Reviewer's comment: *Figure 3 and lines 208-219— The bead separation measurement is insightful, but what was the experimentally measured size of the sub-diffraction beads? How close does this come to the theoretical predictions?*

In Fig. 3, we used an excitation wavelength of λ_{ex} = 850 nm to image 100-nm-diameter polystyrene beads labeled with Rhodamine B (peak emission λ_{em} = 567 nm). For multiphoton order $n = 2$ and NA $\alpha = 1$, the cutoff spatial frequency of an ideal OTF is $k_{\mathrm{c}} = 2\pi\alpha\left(\frac{1}{\lambda_{\mathrm{em}}} + \frac{1}{\lambda_{\mathrm{ex}/n}}\right)$, so the ideal bandwidth-limited (Abbe half-pitch) resolution is $r_{\mathrm{ideal}} = \frac{\pi}{k_{\mathrm{c}}} = \lambda_{\mathrm{ex}}\lambda_{\mathrm{em}}/2\alpha(n\lambda_{\mathrm{em}} + \lambda_{\mathrm{ex}}) \approx 121$ nm. In practice, however, the effective passband is set by sampling: the Nyquist cutoff frequency is $k_{\mathrm{sc}} = \pi/r_{\mathrm{sc}}$, with camera's pixel/scan spacing $r_{\mathrm{sc}} = 131$ nm.

Here we assume that the post-deconvolution OTF is approximately given by a circular flat-top; the corresponding PSF is a jinc-like, $\mathrm{PSF}(r) \propto |J_1(kr)/(kr)|$.

In the right panel in below, the blue curve shows the radial average of the bead indicated by the red box in the left panel. The orange curve is the ideal PSF profile assuming a perfectly flattened OTF of radius k_{sc}, $H_{\mathrm{eff}}(k) = 1$ for $|k| \le \pi/r_{\mathrm{sc}}$. The red curve is a model obtained by convolving a 100-nm-diameter bead (disk) with a jinc PSF while allowing the band limit to vary as $|k| \le \pi/r_{\mathrm{mea}}$. Although the bead size and the post-deconvolution OTF cannot be uniquely separated from a single profile, we estimate that the practical band-limited (Abbe) resolution is $r_{\mathrm{mea}} \approx 154$ nm from the best fit result.

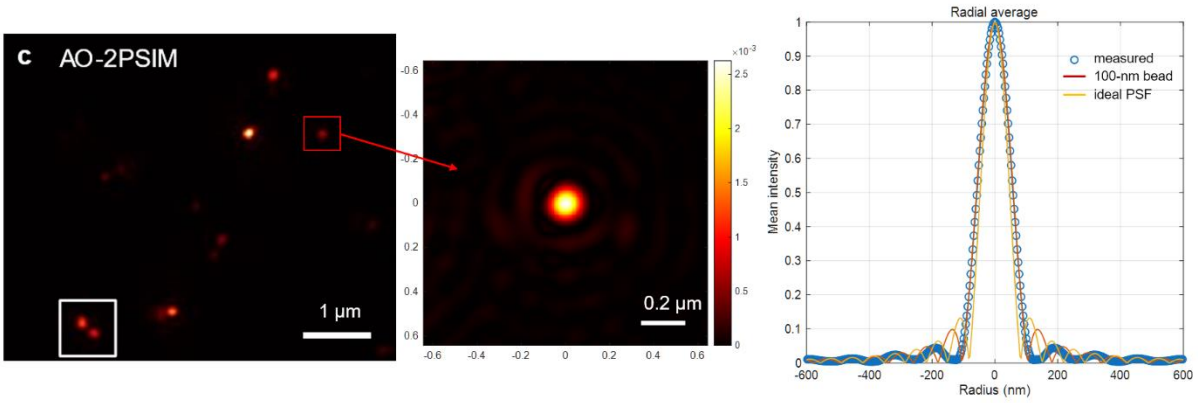

Reviewer's comment: *It would be interesting to see the calculated excitation and emission Zernike modes for some of the samples displayed. How stable are the optimized Zernike modes for a given set of aberrated images?*

Response: Usually, pupil functions are represented as a combination of Zernike modes. However, in our incoherent imaging framework, both excitation and emission OTFs correspond to the autocorrelation of the respective pupil functions. Therefore, Zernike coefficients are not directly accessible. Instead, the goal of our algorithm is to reconstruct effective intensity PSF and OTF for accurate image correction.

To assess stability, we examined the reconstructed PSF/OTF across multiple independent aberrated image sets of the same sample. Then, Pearson correlation coefficients were computed between the reconstructed AO-2PSIM images and the corresponding ideal, noise-free and aberration-free ground truth images. Our results show that the reconstructions are highly reproducible: both the PSF shape and

OTF amplitude/phase remain consistent across repeated measurements or simulations with Pearson-correlation metric.

As shown in Fig. R8a, when SNR exceeds ~4, the reconstructed AO-2PSIM images consistently achieve over 95% correlation with the ideal images, indicating effective recovery of super-resolution. However, below this SNR threshold, the correlation drops significantly.

To further validate the accuracy of the PSF recovery, we analyzed Pearson correlation between the reconstructed and ground-truth excitation and emission PSFs. As shown in Fig. R8b, these correlations steadily improve with increasing SNR and similarly exhibit a clear transition near the super-resolution threshold. This indicates that our reconstruction pipeline can recover both the spatial distribution of the excitation and emission PSFs with high fidelity under low-to-high SNR conditions.

In addition, we quantified the enhancement in image quality achieved by our algorithm by computing both the SNR and signal-to-background ratio (SBR) enhancement factors. These were calculated by comparing AO-2PSIM images to standard 2PSIM images. As shown in Fig. R8c, dual deconvolution in AO-2PSIM significantly improves image quality, yielding up to 6-fold increases in SNR and up to 9-fold increases in SBR under high-SNR conditions. These enhancements provide complementary evidence of the algorithm's effectiveness in suppressing background noise and enhancing signal contrast. All statistical analyses were based on up to 30 independent simulation runs per condition to ensure robust conclusions.

In summary, our extensive simulation results demonstrate that the dual deconvolution AO-2PSIM algorithm reliably recovers super-resolution information under moderate-to-high SNR conditions (SNR > 4), with strong correlations to ideal ground-truth images and PSFs. Although we do not explicitly extract pupil functions with Zernike modes from the intensity PSFs, the stability of the recovered response across varying noise and aberration conditions indirectly supports the stability of the underlying phase corrections.

Reviewer's comment: *Figure S3— Since the idea of isoplanatic patch is mentioned, it could support the concept to calculate the isoplanatic patch size for the image shown. This could be accomplished by applying the optimized Zernike modes to neighboring locations.*

Response: To assess spatial PSF variation across a large field of view, we performed patch-wise PSF estimation on zebrafish spinal cord imaging data. Figure R9a shows the full field-of-view AO-2PSIM image, identical to Fig. 6 in the revised main text. This image was acquired from the hindbrain spinal cord of a 10-dpf zebrafish at a depth of 180 μm. The field of view was divided into a 7×7 grid of 20×20 μm² patches (Fig. R9b), and excitation and emission PSFs were locally estimated from each patch using our dual deconvolution algorithm.

To quantify PSF similarity across the field of view, we calculated the mean-relative error (MRE) between each peripheral PSF and the central reference patch (4,4). The MRE metric is calculated as:

$$\mathrm{MRE}\left(\mathrm{PSF}_{\mathrm{center}}, \mathrm{PSF}_{\mathrm{peripheral}}\right) = \frac{\sum_i \left|\mathrm{PSF}_{\mathrm{center}}(i) - \mathrm{PSF}_{\mathrm{peripheral}}(i)\right|}{\sum_i \left|\mathrm{PSF}_{\mathrm{center}}(i)\right|}.$$

The resulting spatial variation map, displayed as 1 – MRE (Fig. R9c), reveals gradual PSF changes across the field of view, with variations increasing toward the edges and reaching approximately 30% at the periphery.

As an alternative approach to estimate the isoplanatic patch size, we followed the reviewer's suggestion (Fig. R10). From the orange-dotted boxed region in Fig. R9a, we extracted a 10×10 μm² central patch and designated it as the ground-truth patch (blue dotted box). Neighboring regions within the boxed area were then selected at 4 μm intervals. At each location, we independently estimated the excitation and emission PSFs. Each of these PSFs was applied to the original ground-truth region to reconstruct AO-2PSIM images. As expected, image sharpness degraded progressively as PSFs farther from the ground-truth location were used.

To quantitatively determine the isoplanatic patch size from this analysis, we calculated the MRE curve between the ground-truth emission PSF and those retrieved from each neighboring location (Fig. R10b). The resulting 1-MRE profile (red curve) was fitted with a smooth exponential function. The 1/e points of the fitted curve were used to estimate the isoplanatic patch size, yielding an approximate value of 14.8 μm (blue dotted line).

Reviewer's comment: *line 312— A little bit more discussion about other approaches to speed imaging in ISM and alternate detectors (e.g. SPAD cameras) prior to the concluding paragraph could help to strengthen the case for future impact of the work.*

Response: We appreciate the reviewer's suggestion to expand our discussion of approaches for accelerating ISM imaging and incorporating alternative detector technologies. While several of these strategies were already mentioned in the concluding paragraph, such as multifocal illumination and SPAD array detectors, we have now revised the text to further highlight these points:

"Future strategies include enhancing image acquisition speed through methods such as parallel imaging with multifocal illumination[7,34-36] using a digital micromirror device or a liquid-crystal spatial light modulator[19,37-39]. Multifocal sparse sampling could further accelerate image acquisition in combination with sparsity-based high-resolution image reconstruction from incomplete measurements[40]. Additionally, employing SNR-optimized array detectors such as single-photon avalanche diodes (SPAD) array detector[41] may facilitate capturing raw fluorescence maps at a higher SNR, thereby enabling the recovery of the full bandwidth of OTFs."

Reviewer #2

Reviewer's comment: *This manuscript presents a solid advancement in multiphoton super-resolution imaging through the development of a computational adaptive optics (AO) framework based on virtual structured illumination microscopy (SIM). A central innovation is the dual deconvolution algorithm, which iteratively corrects excitation and emission aberrations using Wiener-like updates to solve for three unknowns (i.e., object, excitation OTF, and emission OTF), thus decomposing a complex optimization problem into well-conditioned, tractable subproblems. While the spectral synthesis concept underlying the two-photon SIM implementation is similar to the recently established k-space interpretation of image scanning microscopy in the single-photon regime, the proposed dual deconvolution process represents a novel and effective computational strategy. The use of virtual, rather than real, structured illumination enables the adaptive correction of aberrations, achieving 130 nm lateral resolution at a depth of 180 μm in thick mouse brain tissue. The manuscript is technically sound, with a clearly described algorithmic workflow, comprehensive experimental details, and results that support the applicability of the approach. Overall, this work makes a meaningful contribution to the field and offers a promising computational solution for deep-tissue super-resolution imaging.*

Response: We greatly appreciate the reviewer's thoughtful feedback. We are pleased that the reviewer recognizes the novelty and effectiveness of our dual deconvolution algorithm, as well as the significance of using virtual structured illumination for adaptive optical aberration correction. We also thank the reviewer for acknowledging the clarity of our algorithmic workflow and the technical soundness of our experimental design. These comments reinforce our belief that the proposed method offers a valuable contribution to the field of deep-tissue super-resolution imaging.

Reviewer's comment: *A limitation of the manuscript is the restricted generalizability of the approach. Specifically, the computational adaptive optics framework applies only to virtual structured illumination, which inherently limits imaging speed. Accelerating acquisition would require multifocal scanning strategies, typically involving the capture of hundreds of images, representing a significant weakness compared to hardware AO systems. Additionally, the dual deconvolution algorithm depends on the unique separable structure of the excitation and emission OTFs (Hex and Hem), which is essential for making the problem tractable in this context. Whether this algorithm can be extended to other applications remains unclear and is not discussed in the manuscript.*

Response: We thank the reviewer for this thoughtful and constructive assessment. The comment raises three important aspects: (1) imaging speed, (2) the separable forward model and its generalizability, and (3) potential broader applications. We address them in detail below.

(1) Imaging speed: We agree that imaging speed is a key consideration for the practical use of computational AO. To provide context, we compared our acquisition rate with that of representative hardware AO implementations.

Direct wavefront-sensing AO typically measures the emission wavefront (e.g., with a Shack–Hartmann sensor) using guide stars (well-isolated fluorescent beads or bright point-like emitters), then computes DM voltages (often in Zernike modes). In representative biological preparations (e.g., *Nat Methods* **14**, 869 (2017)), Shack-Hartmann sensor exposures of 0.5–1.5 s per measurement are reported, and the measure–decompose–apply loop is repeated multiple iterations to reach good correction. The number of iterations may change as aberration strength and complexity increases. Typically, end-to-end correction commonly takes several seconds.

Sensor-less AO, which dispenses with a wavefront sensor, acquires a wide-field image at each iteration while sweeping many mode coefficients. A commonly cited bound is least $2N+1$ wide-field images for N Zernike modes, with 7–12 s reported for ~11 modes (*Opt. Express* **16,** 9290 (2008)). In practice, the full optimization can take seconds to minutes depending on the number of modes, signal brightness, and metric.

In our case, with ~1 ms camera exposure per scan position, a fluorescence response function for 100×100-pixel FOV (corresponding to ~12 × 12 μm^2) is acquired in ~10 s. Moreover, as discussed in

the manuscript, multifocal- or instant-SIM schemes (e.g., *Nat Methods* **9**, 749 (2012) and *Nat Methods* **10**, 1122 (2013)) are directly compatible with our acquisition and can shorten it dramatically; for example, a 10×10 focal-spot array would, in principle, provide a ~100× speed-up at the same exposure and SNR.

Considering these factors, our computational approach achieves imaging speeds comparable to practical hardware AO once measurement overheads are included, while uniquely providing super-resolution capability in an aberrating medium.

In fact, the improvement of SNR is a key difference between hardware and computational AO. Hardware AO physically concentrates light into a tighter PSF and thus improves SNR in the raw image, while computational AO including our dual-deconvolution method cannot increase the photon budget and therefore bounded by the acquisition SNR. We view the two approaches as complementary rather than competing: hardware AO first removes dominant aberrations and raise photon budget, after which our spectral synthesis with dual deconvolution recovers residual errors and achieves super-resolution.

We detail the limitations of computational AO and emphasize this hybrid perspective in the Discussion:

"Our proposed computational AO is simpler to implement than hardware AO, but it has drawbacks. Hardware AO increases raw-image SNR by physically concentrating light into a tighter PSF, whereas computational AO cannot increase the photon budget; high-spatial-frequency components of the OTF are attenuated by aberrations and often buried in noise. Although our dual-deconvolution approach recovers high-frequency content more effectively than conventional deconvolution, its gains are ultimately bounded by the acquisition SNR. In practice, the two are complementary: hardware AO first removes dominant aberrations and boosts signal, after which spectral synthesis combined with dual deconvolution recovers residual errors and achieves super-resolution."

(2) Separable forward model and its generalizability: As the reviewer pointed out, our dual deconvolution leverages a separable forward model:

$$F(\mathbf{k}_\mathrm{d}, \mathbf{k}_\mathrm{i}) = H_\mathrm{em}(\mathbf{k}_\mathrm{d}) H_\mathrm{ex}(\mathbf{k}_\mathrm{i}) \Gamma(\mathbf{k}),$$

which ensures the independent estimation of the excitation and emission OTFs, H_ex and H_em. This model assumes a single object plane at a given depth, with H_ex and H_em describing propagation to and from that plane. Multiple scattering and out-of-plane signals are neglected, as is appropriate for two-photon imaging, which inherently provides optical sectioning.

The current formulation considers only main-diagonal elements, corresponding to isoplanatic conditions (possessing shift-invariant aberrations). When spatial variability is stronger (anisoplanatic fields), H_em and H_ex are no longer diagonal matrices. In such cases, a more general three-operator factorization is required:

$$F(\mathbf{k}_\mathrm{d}, \mathbf{k}_\mathrm{i}) = \sum_{\mathbf{k}_\mathrm{i}', \mathbf{k}_\mathrm{d}'} H_\mathrm{em}(\mathbf{k}_\mathrm{d}, \mathbf{k}_\mathrm{d}') \Gamma(\mathbf{k}_\mathrm{d}', \mathbf{k}_\mathrm{i}') H_\mathrm{ex}(\mathbf{k}_\mathrm{i}', \mathbf{k}_\mathrm{i}).$$

To mitigate this complex factorization problem, we adopted patch-wise processing, with patch sizes chosen to match the aberration correlation length. Within each patch, H_ex and H_em can be treated as locally diagonal, allowing stable OTF estimation. This strategy was used in the zebrafish experiment, now presented in Fig. 6 of the revised main text.

(3) Applicability of the proposed algorithm: We have expanded the Discussion section to clarify potential applications beyond the current implementation:

"Our dual-deconvolution concept is not restricted to SIM. It can support single-molecule localization methods (e.g., STORM/SMLM) and STED microscopy[44] by estimating broadened, space-varying PSFs for improved localization. Beyond optics, the dual deconvolution concept extends to an inverse problem in systems wherever a linear response function can be measured."

Reviewer's comment: *Another limitation lies in the biological demonstrations, which are somewhat limited, featuring only a thin cell and a thick sample with only a few xy planes but lacking any 3D volumetric data. While the lateral resolution enhancement is evident, axial resolution and performance are not discussed. As the deconvolution is currently applied only in 2D, the authors may consider discussing potential extensions of the dual deconvolution algorithm to fully exploit super-resolution capabilities in three dimensions. In addition, Supplementary Figure 3, which presents zebrafish imaging, appears more compelling than Figure 5, as it shows a more pronounced improvement after computational AO correction and effectively demonstrates the method's ability to address challenging cases with spatially varying aberrations.*

Response: We thank the reviewer for raising the perspective of extending the dual deconvolution algorithm to 3D imaging. The simple and straightforward approach would be to perform depth scanning, measure the fluorescence response function $f(\mathbf{r}_\mathrm{d}, \mathbf{r}_\mathrm{i}, z)$ at each depth z, apply dual deconvolution slice by slice, and then construct a 3D stack image. Another possible direction would be to consider a true 3D dual deconvolution of $f(\mathbf{r}_\mathrm{d}, \mathbf{r}_\mathrm{i}, z)$ that simultaneously accounts for the 3D OTFs and the volumetric target distribution. While conceptually simple, this approach would demand substantial computational and experimental resources, including depth-dependent modeling of both excitation and emission PSFs.

Alternatively, one might attempt to retrieve depth information from a single-depth response function $f(\mathbf{r}_\mathrm{d}, \mathbf{r}_\mathrm{i})$ acquired at the focal plane. This idea is analogous to digital refocusing in coherent imaging (e.g., digital holography). However, in incoherent imaging, the lack of phase information prevents direct application. Moreover, because the 3D intensity PSF is symmetric above and below the focal plane, out-of-focus signals cannot easily be distinguished between the +z and –z directions. To break this axial symmetry, engineered PSFs such as those with astigmatic aberration (*Proc. Natl. Acad. Sci. U.S.A.* **109,** 7175 (2012)) or a double-helix structure (*Opt. Lett.* **31,** 181 (2006)) may be adopted. Nevertheless, the implementation and validation of such 3D extensions are beyond the scope of the present study and merit a dedicated investigation.

We have added the following sentence to the Discussion to reflect this future direction:

"As an intriguing future perspective, the dual deconvolution framework could be extended to three dimensions by incorporating depth-dependent PSFs, such as those engineered with astigmatic aberration[42] or a double-helix structure[43]."

In line with the reviewer's suggestion, we have also moved the previous Supplementary Fig. S3 (zebrafish imaging) to the main text as the new Fig. 6.

Reviewer's comment: *(1) The data processing speed is not discussed, including the spatially varying iterations for multiple regions.*

Response: In our current implementation, the reconstruction of the large field-of-view zebrafish image shown in Fig. 6 (145×145 μm^2) took a total of 1,886 seconds in processing 49 patches entirely on the CPU. This corresponds to approximately 38 seconds per patch (size of each patch of 20×20 μm^2). The computations were performed on a workstation equipped with an Intel(R) Core(TM) i9-11900K @ 3.50GHz processor and 128 GB RAM. We expect further acceleration through GPU-based parallelization and optimized implementation in future work. We added these details to the revised manuscript (in Methods).

Reviewer's comment: *(2) Line 100, ki is not well defined*

Response: $\mathbf{k}_\mathrm{i}$ is defined by adding "…with a wavevector $\mathbf{k}_\mathrm{i}$".

Reviewer's comment: *(3) Line 104, alpha (numerical aperture?) is not defined.*

Response: α is defined by "…is given by αk_{em}, where α is the numerical aperture and $k_{\mathrm{em}} = 2\pi/\lambda_{\mathrm{em}}$,…"

Reviewer's comment: *(4) Fig. 5(g), the dash lines 1-5 seem off from the spine neck.*

Response: The positions of dashed lines are correct. The lower panel shows a saturated image of spine neck #1, in which the dimly dendritic spine neck is clearly visualized.

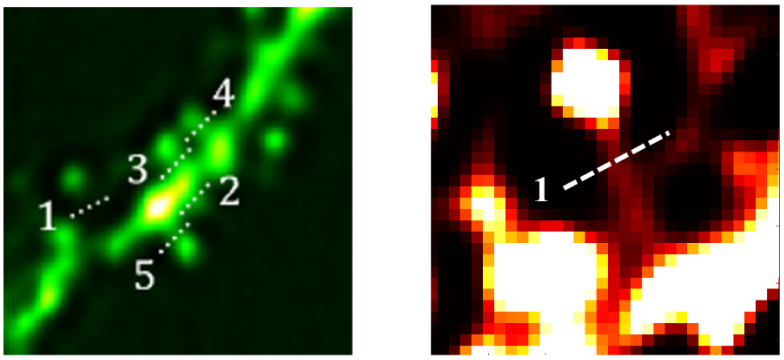

Reviewer #3

Reviewer's comment:

 # Advantages
1. Interesting idea. The author proposed a dual deconvolution computational aberration correction (AO) algorithm that corrects for aberrations in both excitation and emission in multiphoton deep-tissue structured illumination microscopy (SIM).
2. No additional hardware required. The proposed method doesn't require complex wavefront shaping or sensing devices.
3. Good experimental results. The improvements in aberration correction and resolution are clearly demonstrated.
4. Code and data are available online, which will benefit the community.

Response: We sincerely thank the reviewer for the positive and encouraging feedback. We are pleased that the reviewer recognizes the novelty of our dual-deconvolution computational aberration correction approach, as well as its ability to address both excitation and emission aberrations without requiring additional hardware. We also appreciate the acknowledgment of our experimental validation and the potential value of openly sharing our code and data. These comments are greatly appreciated and will help guide future extensions and improvements of our work.

Reviewer's comment:

 # Weakness
1. Computational AO methods generally suffer from low SNR, especially when applied to deep tissue imaging. All experimental results provided by the authors have very high SNR. The paper lacks analysis of how SNR affects the reconstruction quality.

Response: We thank the reviewer for raising this important concern regarding the impact of SNR on reconstruction performance, particularly in deep-tissue imaging. To address this point, we performed extensive simulations under varying noise conditions and systematically analyzed the robustness of our AO-2PSIM algorithm. The results are now included in the Supplementary Information (SI, Sections 4).

To investigate dual-deconvolution performance, we conducted simulations across a range of noise levels while maintaining aberration strength and complexity (Fig. R4). Independent excitation and emission pupil functions were numerically generated using Zernike modes up to N=30 (piston and tilt excluded), yielding 505 modes in total. From the corresponding OTFs, fluorescence response functions were simulated at various noise levels, and AO-2PSIM images were reconstructed via dual deconvolution. As the SNR of the 2PSIM images decreased, the recoverable high-frequency information in the effective OTFs diminished (as shown in the PTF images in Fig. R4), leading to reduced fidelity in both the recovered and corrected PSFs. The algorithm maintains reasonable performance down to SNR≈4 (measured from the 2PSIM images), consistent with SNR>4 estimated for the dataset in Fig. 4h (main text). Below this level, the fidelities of both the recovered target images and the PSFs degrade.

Fourier ring correlation (FRC) curves obtained from 2PSIM images at various SNR conditions show resolution degradation with increasing noise before aberration correction (Fig. R5a). In contrast, FRC curves from AO-2PSIM images mostly demonstrate higher cut-off frequencies (Fig. R5b). The direct visualization of these cut-off frequencies (Fig. R5c) shows the bandwidth recovery capability of the dual deconvolution method.

To further validate this, we performed 10 independent simulation runs at each SNR level and calculated SNR-enhancement factors and resolutions. The results show that our method improves SNR by up to 8-fold (Fig. R5d), and super-resolution (cut-off frequency > $3\alpha k_{em}$, i.e., resolution < $\lambda_{em}/3\alpha$) is achievable at SNR>4. These quantitative SNR-resolution correlations clarify the performance of dual deconvolution across diverse noise and aberration conditions.

Reviewer's comment: *2. The reconstruction quality in SIM algorithms is highly dependent on the modulation depth or contrast of the illumination pattern, which tends to degrade after propagating through a scattering medium. How do the authors address this issue? And how significantly does this degradation affect the final reconstruction quality?*

Response: Conventional SIM relies on illuminating modulation patterns over a wide field-of-view. These patterns are inherently phase-sensitive, and thus their modulation contrast degrades, and their spatial phase is shifted when propagating through deep scattering or aberrating media. Furthermore, scattering also increases out-of-focus background signals, which further reduces SNR of raw images. Here, the reduction in modulation contrast is described by the modulation transfer function (MTF), while spatial shifts of the modulation patterns correspond to phase variations in the phase transfer function (PTF).

To mitigate these deteriorating effects, our approach addresses the problem on two complementary levels:

(1) Physically robust excitation: We employed two-photon excitation with point scanning and synthesized virtual structured illumination, enabling deeper imaging with higher SNR than conventional one-photon and wide-field illumination SIM. Multiphoton excitation spatially confines emission signal inherently to an excitation focal volume such that it effectively suppresses background noise and maintains high-contrast virtual illumination pattern even in scattering samples (*Nat. Commun.* **16**, 5386 (2025)).

(2) Computationally robust reconstruction: Even when residual aberrations remain, our dual-deconvolution algorithm explicitly models both excitation and emission aberrations during post-processing. Conventional SIM deconvolution operates on the synthesized SIM spectrum, $\tilde{I}_{\mathrm{SIM}}(\mathbf{k})$, which suffers from deep local minima in the effective MTF, $\tilde{H}_{\mathrm{SIM}}(\mathbf{k})$, caused by aberrations. It leads to severe noise amplification during normalization (see Fig. R5). In contrast, our dual-deconvolution method deconvolves the fluorescence response function, $F(\mathbf{k}_{\mathrm{d}}, \mathbf{k}_{\mathrm{i}})$ before SIM synthesis, using a two-dimensional Wiener-like filter:

$$W_{\mathrm{DCON}}(\mathbf{k}_{\mathrm{d}}, \mathbf{k}_{\mathrm{i}}) = \frac{H_{\mathrm{em}}^{*}(\mathbf{k}_{\mathrm{d}}) H_{\mathrm{ex}}^{*}(\mathbf{k}_{\mathrm{i}})}{|H_{\mathrm{em}}(\mathbf{k}_{\mathrm{d}}) H_{\mathrm{ex}}(\mathbf{k}_{\mathrm{i}})|^{2} + e}.$$

This operation effectively removes phase-induced destructive interference (through conjugate phase correction) and equalizes amplitude suppression (through MTF compensation). After phase removal, the effective MTF to be corrected reduces to a magnitude-only convolution (see Fig. R5c). Thus, an effective MTF for dual deconvolution becomes $\mathrm{MTF}_{\mathrm{DCON}}(\mathbf{k}) = (|H_{\mathrm{em}}| * |H_{\mathrm{ex}}|)(\mathbf{k})$, thereby avoiding phase-induced nulls that plague conventional single-OTF-based deconvolution on $\tilde{I}_{\mathrm{ISM}}$. Consequently, the dual-deconvolution approach enhances both contrast and stability of the reconstructed SIM images, even under significant aberration or scattering.

Reviewer's comment: *3. From a practical standpoint, also as an echo to earlier points, the proposed algorithm is a sophisticated but still blind deconvolution/non-convex optimization method. This kind of approach can be prone to getting trapped in local minima, especially when dealing with complex OTF shapes. The authors highlight that their method requires no prior knowledge of the PSF (as noted in lines 425–426 and 431), and that it uses only simple regularization (line 360, section "Dual deconvolution algorithm"). Given this, is there a risk that the algorithm may fail to recover the PSF in certain conditions? I would expect to see examples where the method struggles, such as particular types of excitation/emission PSFs or sample structures that may pose challenges.*

Response: Conventional blind deconvolution relies on a single measured image whose spectrum can be expressed as the product of the object spectrum and the OTF. The joint estimation of the object and

OTF spectra is mathematically underdetermined, since their overlapping frequency components result in multiple feasible solutions in the absence of prior knowledge or constraints.

In contrast, our dual-deconvolution approach utilizes the fluorescence response function, $F(\mathbf{k}_\mathrm{d}, \mathbf{k}_\mathrm{i})$, which captures the object spectra under multiple $\mathbf{k}_\mathrm{i}$. The use of multiple measurements removes the ambiguity between the object and OTF spectra and transforms the problem into a well-determined system.

If $F(\mathbf{k}_\mathrm{d}, \mathbf{k}_\mathrm{i})$ is represented in in discrete form as an $N \times N$ fluorescence response matrix, each element is given by

$$F[\mathbf{k}_\mathrm{d}, \mathbf{k}_\mathrm{i}] = H_\mathrm{em}[\mathbf{k}_\mathrm{d}]\Gamma[\mathbf{k}_\mathrm{d} + \mathbf{k}_\mathrm{i}]H_\mathrm{ex}[\mathbf{k}_\mathrm{i}].$$

Here, the unknowns are the excitation and emission OTFs, $H_\mathrm{em}[\mathbf{k}_\mathrm{d}]$ and $H_\mathrm{ex}[\mathbf{k}_\mathrm{i}]$ (each of length N), and the object spectrum Γ (of length $2N + 1$), yielding $3N + 1$ unknowns. Meanwhile, the number of equations equals the total number of elements, N^2, meaning that the system becomes overdetermined for sufficiently structured objects.

However, if the object spectrum lacks diversity, the equation becomes linearly dependent, and the solution becomes underdetermined. For example, in the extreme case of a spatially uniform fluorophore distribution whose spectrum contains only DC component, Γ effectively behaves as an identity function. In this case, the equations become linearly dependent, and the solution becomes underdetermined. In practice, we note that most biological samples possess rich spatial features that ensure adequate spectral diversity, making the system well-conditioned.

In terms of optimization stability, convergence issues arise primarily under low-SNR conditions, especially in high-frequency regions where the OTF magnitude approaches zero. In such cases, appropriate regularization (Wiener-like in our implementation) is crucial to stabilize the inversion and suppress noise amplification. With sufficient SNR and object diversity, however, our simulations and experimental results demonstrate stable convergence without the need for any priors or heavy regularization.

In response to the reviewer's suggestion, we performed simulations to demonstrate that our dual-deconvolution method can successfully reconstruct both the PSFs, and the object even when the aberrations are strong and highly complex. The simulations results presented in Figs. R6-7 support the convergence stability of the dual deconvolution algorithm.

(1) Analysis of aberration strength

To quantify dual-deconvolution performance as aberration strength increases, we conducted a simulation study under ideal noise-free conditions using Zernike modes up to N=30 (Fig. R6). The Zernike-coefficient magnitudes were systematically scaled to control aberration strength, and reconstruction quality was assessed by the Pearson correlation (PC) between the recovered and ground-truth PSFs. As aberration strength increases, PC values decrease, consistent with reduced high-frequency support in the reconstructed OTFs. At higher aberration levels, the loss of high-frequency content primarily limits the achievable resolution and renders fine structural details.

(2) Analysis of aberration complexity

We extended the analysis to aberration complexity by increasing the number of Zernike modes from N=30 to N=120 (Fig. R7). As complexity increased, the recovered OTFs exhibited increasingly complex phase structures, and PC between reconstructed and ground-truth images steadily declined, indicating a reduction in resolution and accuracy of retrieved OTFs and PSFs.

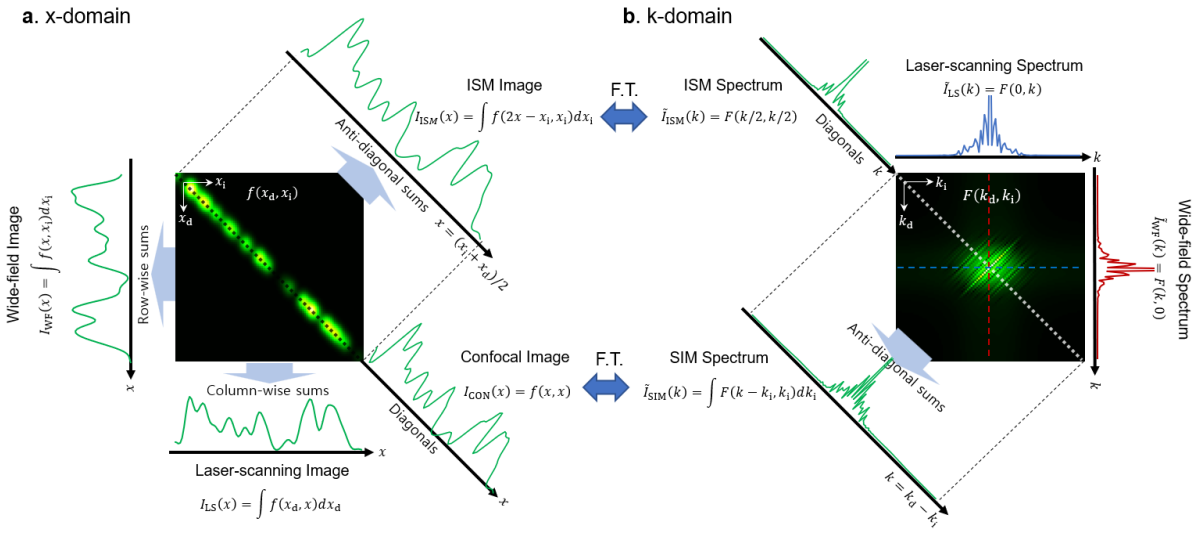

Fig. R1 | Comprehensive comparison of image reconstruction methods from the response matrix. This figure illustrates the fundamental differences between various image reconstruction approaches in both spatial (x-domain) and spatial frequency (k-domain) representations. **a,** Image reconstruction in x-domain. From the measured response function $f(x_d, x_i)$, images are reconstructed via simple kernels: wide-field (WF)—sums over all illumination positions, capturing all emitted light regardless of excitation location; laser-scanning (LS)—sums over all detection positions, integrating signal from point illumination; confocal (CON)—extracts main-diagonal slice, combining spatial filtering in both excitation and detection; ISM (pixel reassignment)—sums along anti-diagonals. **b,** Spectra of the corresponding Fourier domain images in k-space: WF spectrum—slice along detection axis (k_d); LS spectrum—slice along illumination axis (k_i); SIM/CON spectrum—anti-diagonal projection; ISM spectrum—main-diagonal slice.

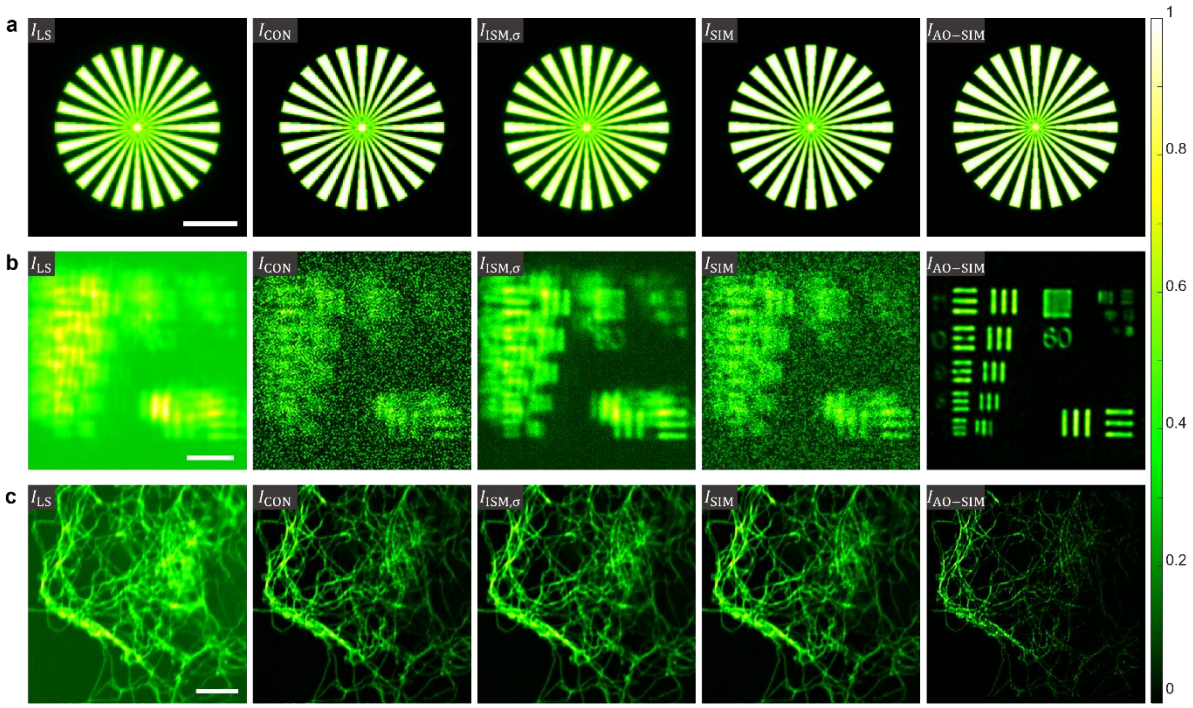

Fig. R2 | Comparative image reconstructions from fluorescence response functions. This figure demonstrates practical implementations of five imaging modes on identical datasets **a**, Simulation dataset (aberration-free, noise-free) reconstructed from a response function, showing theoretical limits of each reconstruction method under ideal conditions. **b**, Experimental dataset from Fig. 4f-k (main text). **c**, COS-7 cell specimen from Fig. 5 (main text). Here, five reconstruction modes are compared: laser scanning (I_{LS}), confocal (I_{CON}), pixel-reassignment (I_{ISM}), SIM spectral-synthesis (I_{SIM}), and AO-processed AO-SIM ($I_{\mathrm{AO-SIM}}$). In **b** and **c**, $I_{\mathrm{ISM},\sigma}$ denotes ISM images reconstructed with an optimal Gaussian loose-confocal filter ($\sigma = 0.3$ μm). All scale bars indicate 3 μm.

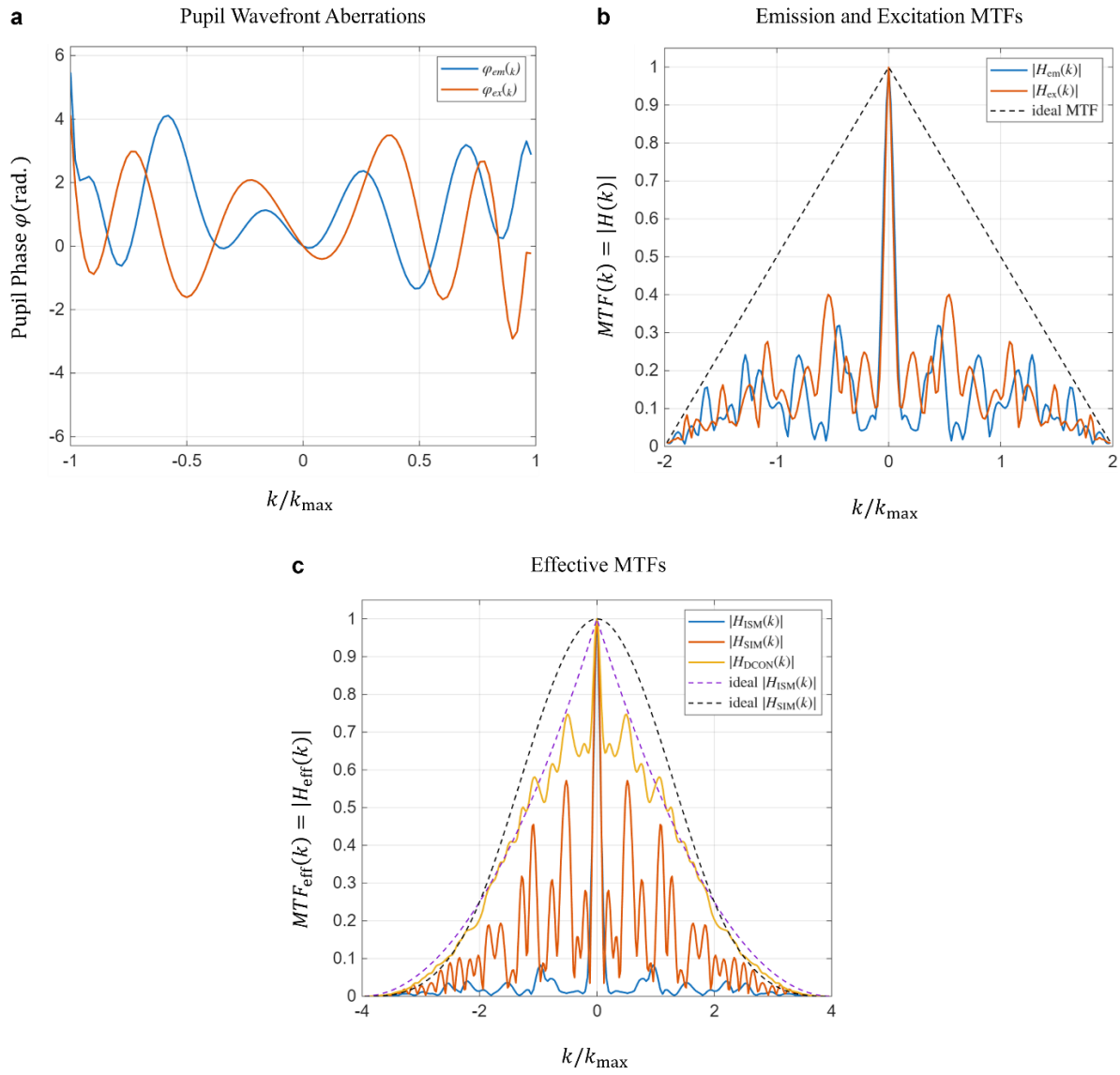

Fig. R3 | Pupil aberrations and effective transfer functions. a, Randomly generated phase distributions for emission and excitation paths (1D slice shown for clarity), representing typical sample-induced aberrations encountered in deep tissue imaging. Here, the numerical aperture $\alpha = 1$ and $k_{max} = k_{em} = k_{ex}$. **b,** Single-pass modulation transfer functions (MTFs) correspond to **a,** $|H_{em}(k)|$ and $|H_{ex}(k)|$. **c,** Effective MTFs comparison for ISM ($H_{ISM}(k) = H_{em}\left(\frac{k}{2}\right) H_{ex}\left(\frac{k}{2}\right)$), SIM ($H_{SIM} = H_{em} * H_{ex}$), and dual deconvolution ($|H_{DCON}(k)| = |H_{em}(k)| * |H_{ex}(k)|$). The ideal $|H_{ISM}(k)|$ and ideal $|H_{SIM}(k)|$ show effective MTFs of ISM and SIM without aberrations, respectively. Aberrations create deeper local suppressions in $|H_{ISM}|$ than in $|H_{SIM}|$, whereas dual deconvolution alleviates phase-induced minimum and yields a broader, better-conditioned passband.

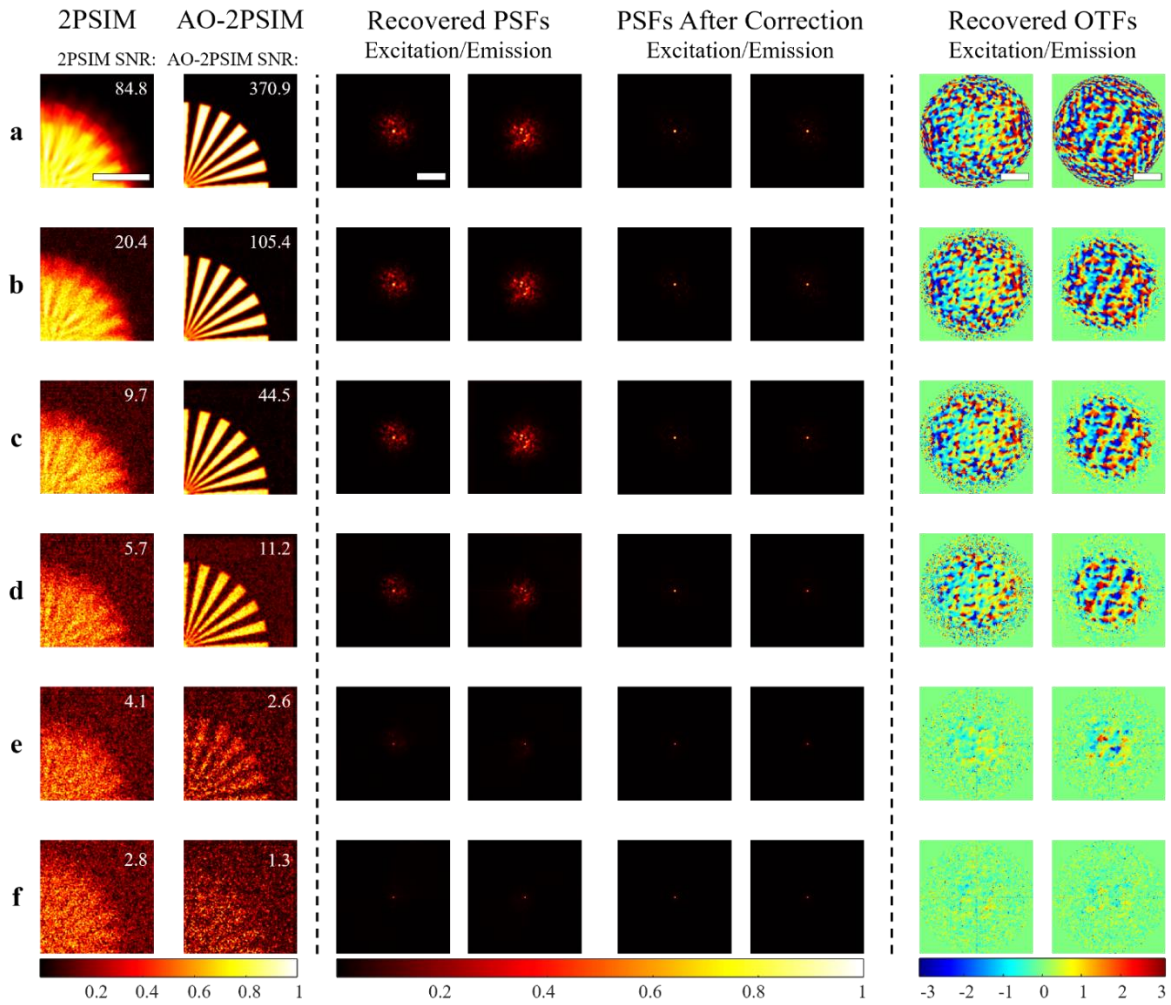

Fig. R4 | Noise analysis demonstrating robustness of AO-2PSIM reconstruction. This comprehensive analysis evaluates algorithm performance across different noise levels while maintaining constant aberration strength and complexity, with rows **a-f** showing increasing noise levels from SNR 30.4 to 3.9. The first two columns display 2PSIM images before correction and AO-2PSIM images after correction with dual deconvolution, respectively, while the third column shows estimated excitation and emission PSFs revealing progressive degradation, and the fourth column presents recovered phase transfer functions (PTFs) that indicate noise-dependent reconstruction fidelity. Scale bars indicate 5 μm in image panels (**a, b, d**). Scale bars in PTF panels indicate emission/excitation cutoff frequencies of αk_{ex} and αk_{em}, respectively.

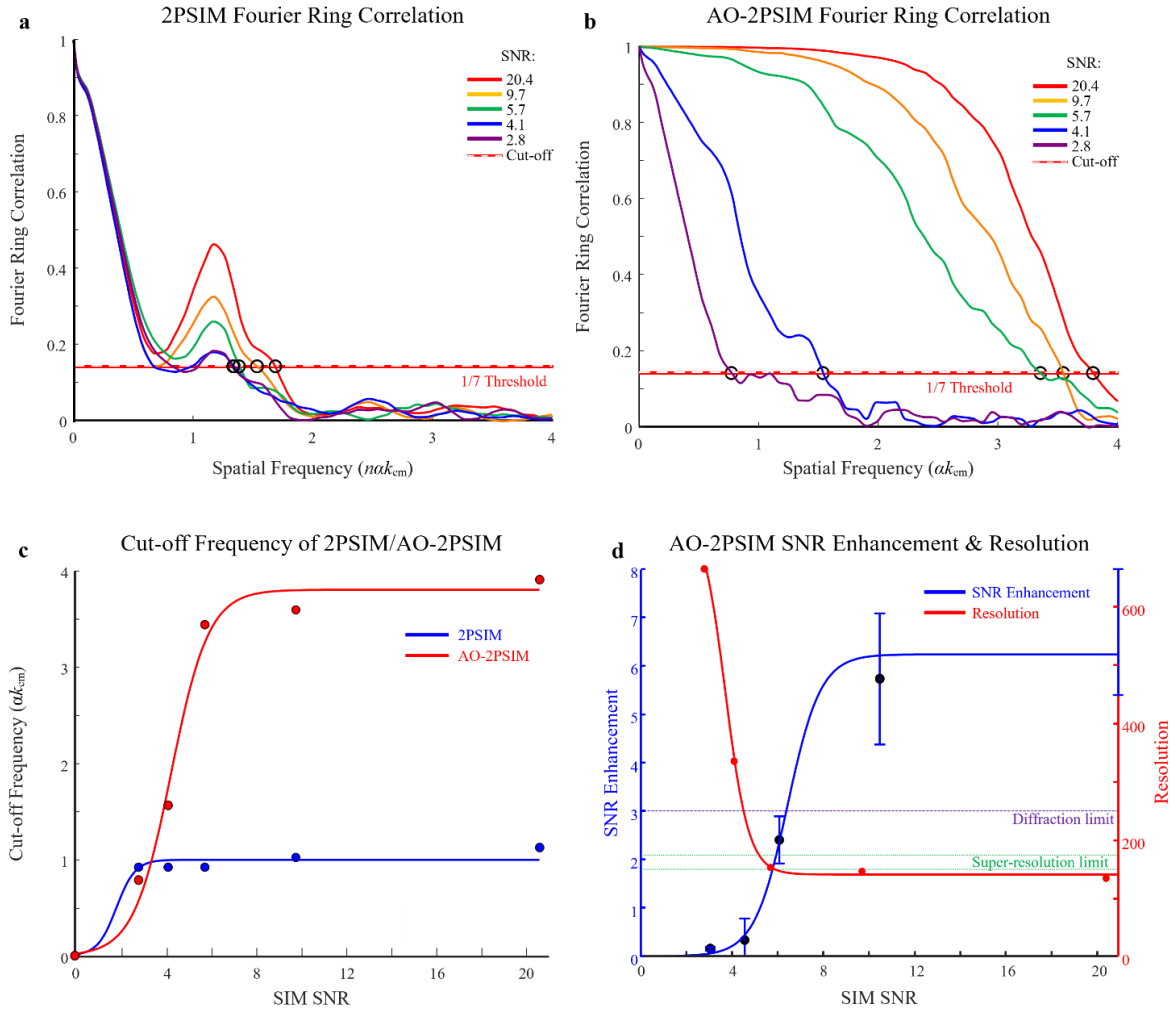

Fig. R5 | Quantitative Fourier Ring Correlation (FRC) analysis of resolution and SNR enhancement in AO-2PSIM under varying noise conditions. a, FRC curves obtained from 2PSIM images at various SNR conditions, where the cut-off 1/7 line indicates the cut-off frequencies that define the resolution limit. **b,** FRC curves obtained from AO-2PSIM demonstrate higher cut-off frequencies compared to those of 2PSIM at various SNR conditions. **c,** Direct visualization of cut-off frequencies obtained from **a** and **b. d,** Combined bar-line plots showing SNR enhancement factors and resolution values, with means and standard deviations obtained from 10 simulation runs at the same SNR but with different aberration and noise fluctuations.

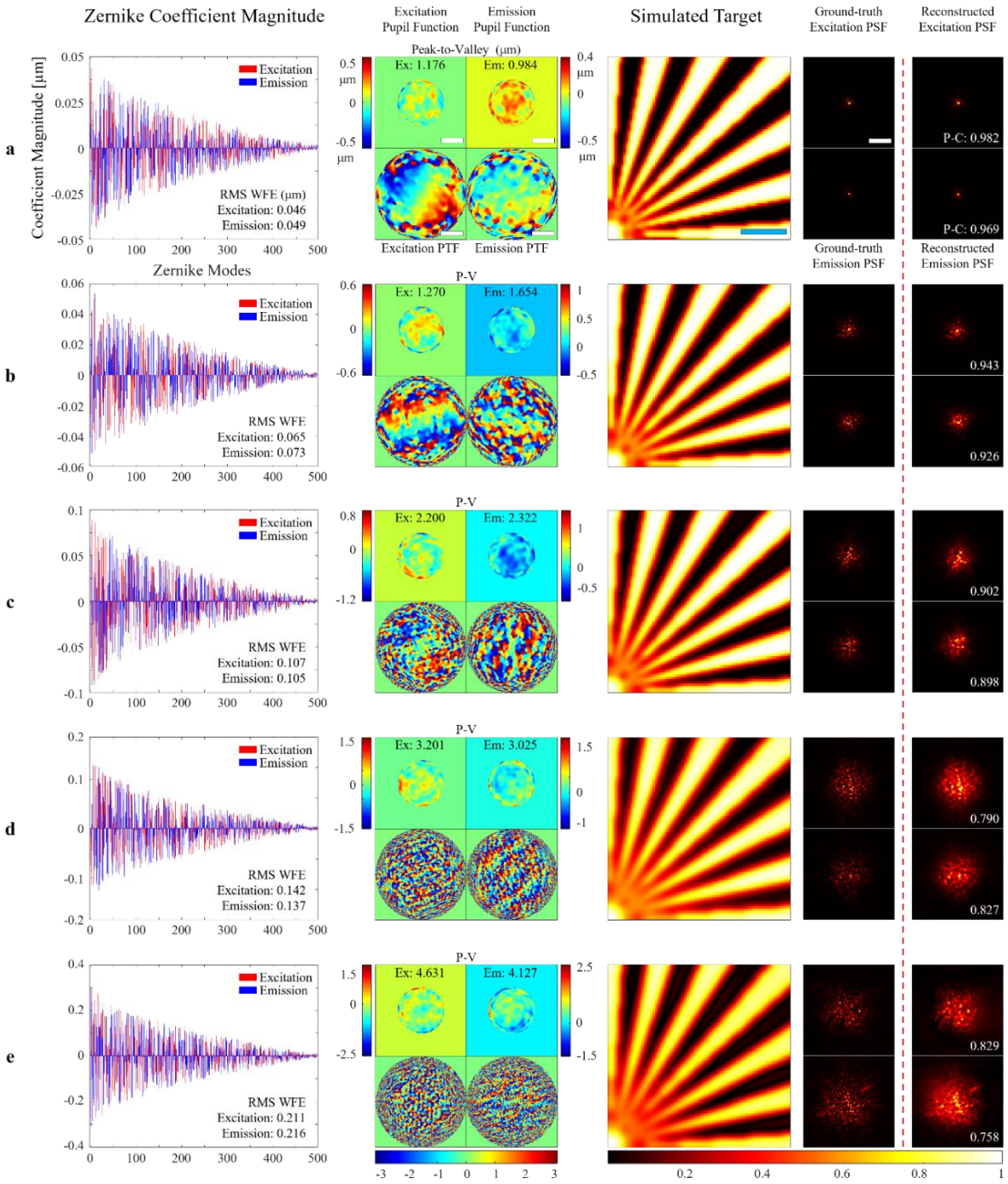

Fig. R6 | Simulation performance of dual-deconvolution algorithm under increasing aberration strength. Rows **a-e** show increasing aberration strength. Columns display Zernike coefficients for independently generated excitation and emission pupil functions, the corresponding pupil phase maps and OTF phase maps, AO-2PSIM reconstructions of a Siemens star target, and recovered PSFs alongside ground truth PSFs. RMS WFE: RMS wavefront error calculated from each pupil phase map. P-V: Peak-to-valley calculated from each pupil phase map. P-C: Pearson correlation coefficient between recovered and ground-truth PSFs. Scale bars: AO-2PSIM, 1.5 μm; PSF, 5 μm. Scale bars in the pupil and OTF maps indicate the excitation/emission cutoffs αk_{ex} and αk_{em}.

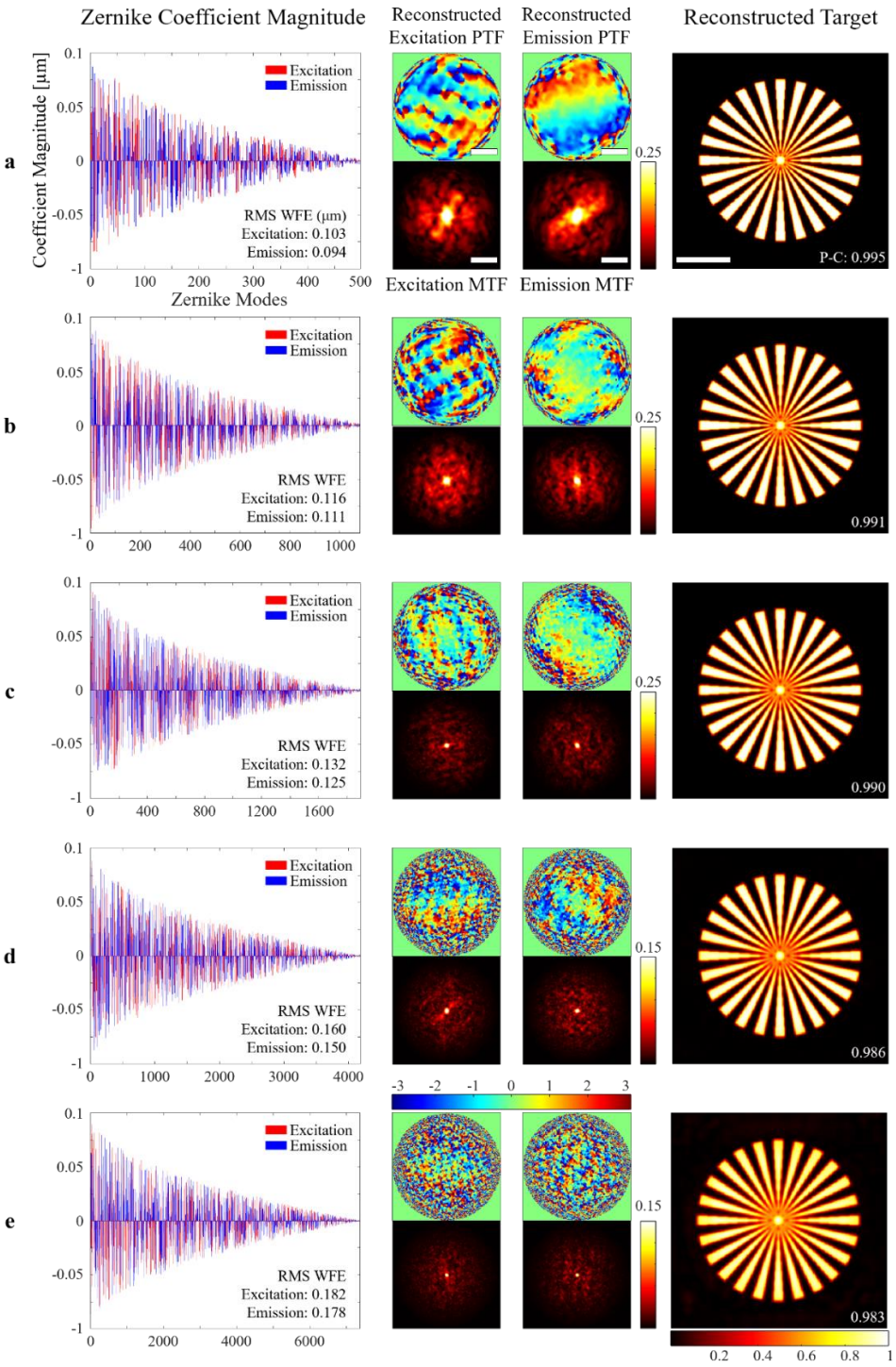

Fig. R7 | Simulation performance of dual deconvolution under increasing aberration complexity. Panels **a-e** show simulations with different numbers of Zernike modes, using independently generated excitation and emission pupil functions. Across **a-e,** simulations were repeated with Zernike modes progressively increased from 30 to 120 while the Zernike coefficient magnitudes were kept constant. Zernike modes up to 30 were used in **a,** and the RMS wavefront error values for the excitation and emission pupil functions are indicated as inset values. The two columns to the right display the ground-truth excitation phase transfer function (PTF) and modulation transfer functions (MTF) for excitation and emission, respectively. The adjacent column shows the reconstructed AO-2PSIM image. Pearson correlation values calculated between reconstructed and ground-truth AO-2PSIM images are shown in the figures. Scale bars in the

excitation PTF/MTF represent αk_{ex}. Scale bars in the emission PTF/MTF represent αk_{em}. Scale bar in the AO-2PSIM image represents 5 μm.

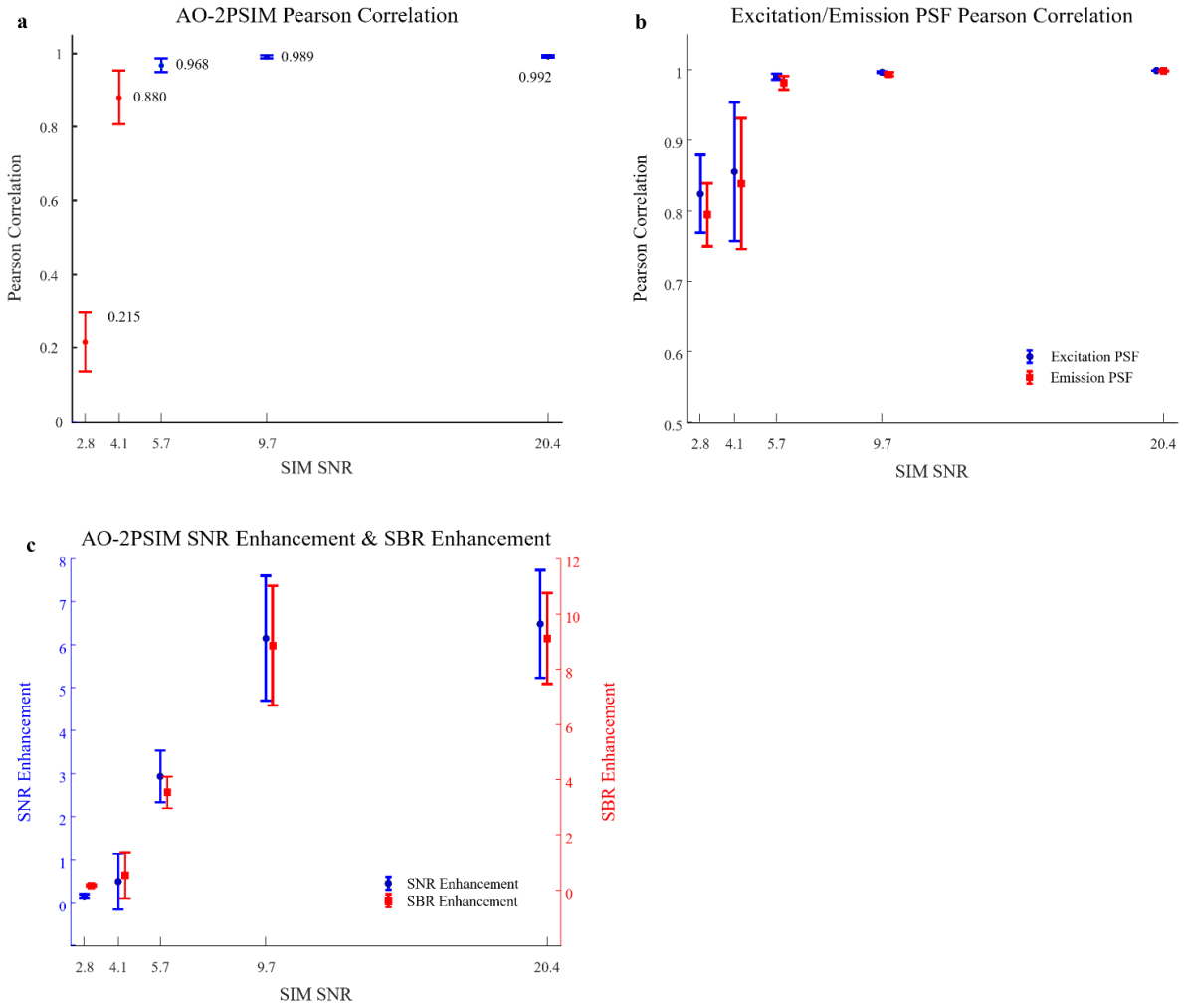

Fig. R8 | Performance evaluation of the dual deconvolution algorithm under aberration and noise. **a**, Pearson correlation between reconstructed and ideal AO-2PSIM images under various SNR conditions. Super-resolution reconstruction becomes reliable (≥95% correlation) when SNR exceeds 4. **b**, Correlation of reconstructed excitation/emission PSFs with ground truth, showing consistent improvement beyond the SNR threshold. **c**, SNR and SBR enhancement factors (AO-2PSIM vs. 2PSIM) demonstrating up to 6× and 9× improvements, respectively, under high-SNR conditions. All metrics are averaged over 30 simulation runs.

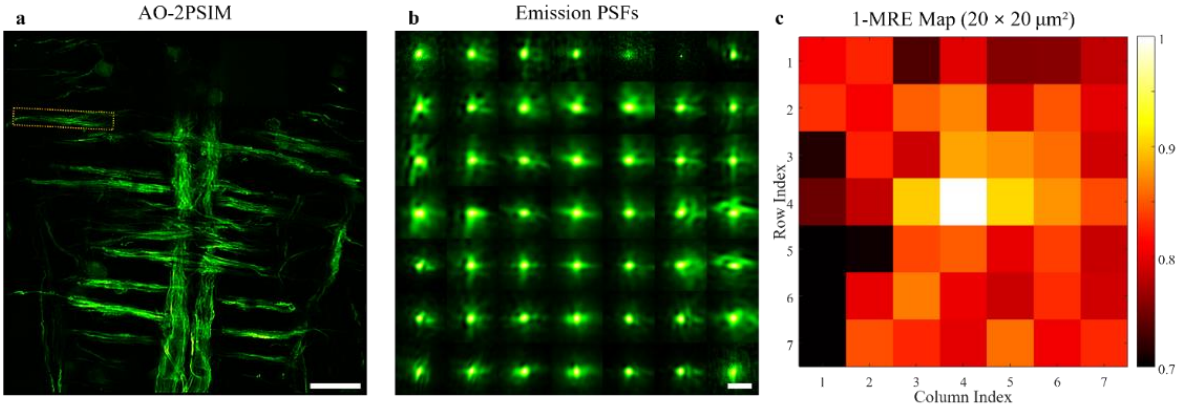

Fig. R9 | Estimation of spatially varying PSFs over a large field of view from spinal cords of zebrafish. a, Identical AO-2PSIM figure from Fig. 6 (main text) is shown. Panel **b** shows emission PSFs reconstructed from panel **a. c,** Mean-relative error (MRE) values were computed between the PSF obtained from the central patch and peripheral PSFs in panel **b,** which is represented as a 1-MRE map. Each individual patch corresponds to the emission PSF shown in **b,** represented by column and row indices.

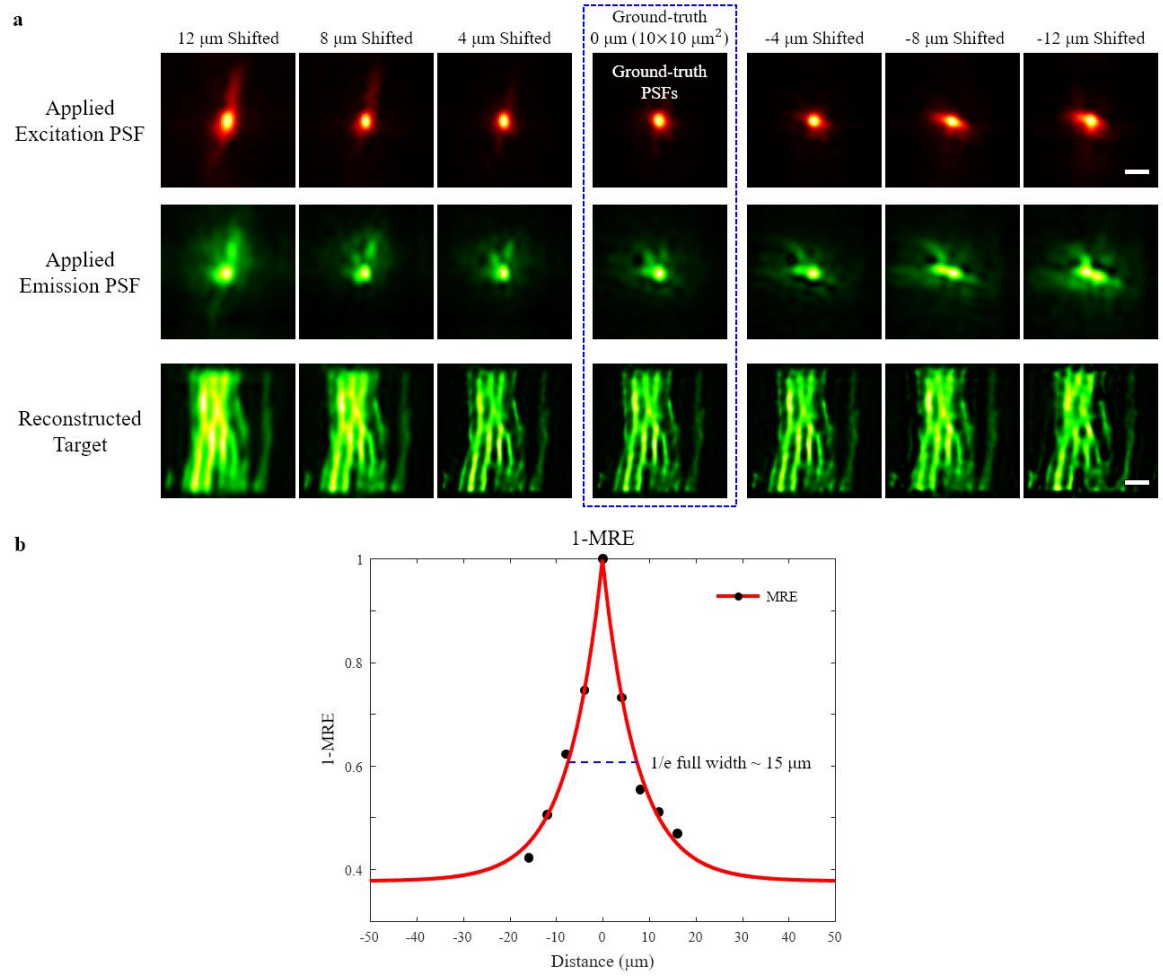

Fig. R10 | Evaluation of isoplanatic patch size based on MRE metric. a, A ground-truth patch was first defined, and the reconstruction was performed on this region using excitation/emission PSFs estimated from neighboring regions. The ground-truth patch (0 μm offset) is represented in blue dotted box. PSFs are then estimated from neighboring patches, which are displayed in the first and second rows, laterally shifted by 4 μm each. All these PSFs were applied to the original

ground-truth region to reconstruct AO-2PSIM images, which are displayed in the third row. Here, scalebars represent 2 μm. **b,** A 1-MRE plot (red fitted curve) shows the evaluation results of spatial PSF variance from **a.** The $1/e$ full width was measured to estimate the rough isoplanatic patch size.